C. R. Physique 11 (2010) 641–649

Contents lists available at ScienceDirect

Comptes Rendus Physique

www.sciencedirect.com

Physics / Solids, fluids: mechanical and thermal properties

3D imaging in material science: Application of X-ray tomography

Luc Salvo [a,*], Michel Suéry [a], Ariane Marmottant [b], Nathalie Limodin [c], Dominique Bernard [d]

[a] Université de Grenoble, laboratoire SIMAP, groupe GPM2, ENSE3, site ampère, 101, rue de la physique, BP 46, Saint Martin d'Hères, France
[b] AICAN Rio TINTO, 725, rue Aristide-Berges, ZI centr'alp, BP 27, 38341 Voreppe, France
[c] Laboratoire de mécanique de Lille – CNRS UMR 8107, École centrale de Lille, boulevard Paul-Langevin, 59655 Villeneuve d'Ascq cedex, France
[d] CNRS, université de Bordeaux, ICMCB, 87, avenue du Dr. A. Schweitzer, 33608 Pessac cedex, France

ARTICLE INFO

Article history:
Accepted 15 December 2010
Available online 21 January 2011

Presented by Yves Bréchet

Keywords:
Aluminium
Metallic foam
Solidification
X-ray micro-tomography

Mots-clés :
Aluminium
Mousse métallique
Solidification
Micro-tomographie aux rayons X

ABSTRACT

In the field of materials science, it is common to relate mechanical or physical behaviour to microstructure in order to optimize materials. Usually the observation of the microstructure is made using an optical or electronic microscope to obtain images in two dimensions. However, the measurable parameters in 2D are limited and often the techniques involved to obtain these images are destructive. Thanks to X-ray micro-tomography it is possible to overcome these two difficulties. The purpose of this article is to show the enormous contribution of this tool in the understanding and the modelling of some physical phenomena involved in aluminium alloys.

RÉSUMÉ

Dans le domaine de la science des matériaux, il est fréquent de relier leur comportement physique ou mécanique à leur microstructure afin d'optimiser ces matériaux. Habituellement l'observation de la microstructure se fait à l'aide de microscopes (optique ou électronique) qui permettent d'obtenir des images en 2 dimensions. Cependant les grandeurs mesurables en 2D sont limitées et souvent les techniques mises en œuvre pour réaliser ces images sont destructives. Grâce à la micro-tomographie aux rayons X il est possible de surmonter ces deux difficultés. L'objet de cet article est de montrer l'apport énorme de cet outil à la compréhension et à la modélisation de phénomènes physiques intervenant dans les alliages d'aluminium.

1. Introduction

In the field of materials science it is often necessary to make correlations between the properties of materials and their microstructure. In the case of metallic materials, the microstructure is usually correlated to defects defined as perturbations in comparison with the perfect single crystal and to the presence of alloying elements. These defects are thus vacancies, dislocations, grain boundaries, pores and cracks, and in the case of alloys, one can find foreign atoms in solid solution, precipitates, dispersoïds and second phases in addition to the previously mentioned structural defects. These various microstructural features can form during elaboration, shaping and use of the materials all along their life time. The relevant

* Corresponding author.
E-mail addresses: luc.salvo@simap.grenoble-inp.fr (L. Salvo), michel.suery@simap.grenoble-inp.fr (M. Suéry), ariane.marmottant@riotinto.com (A. Marmottant), nathalie.limodin@ec-lille.fr (N. Limodin), bernard@icmcb-bordeaux.cnrs.fr (D. Bernard).

1631-0705/$ – see front matter
doi:10.1016/j.crhy.2010.12.003

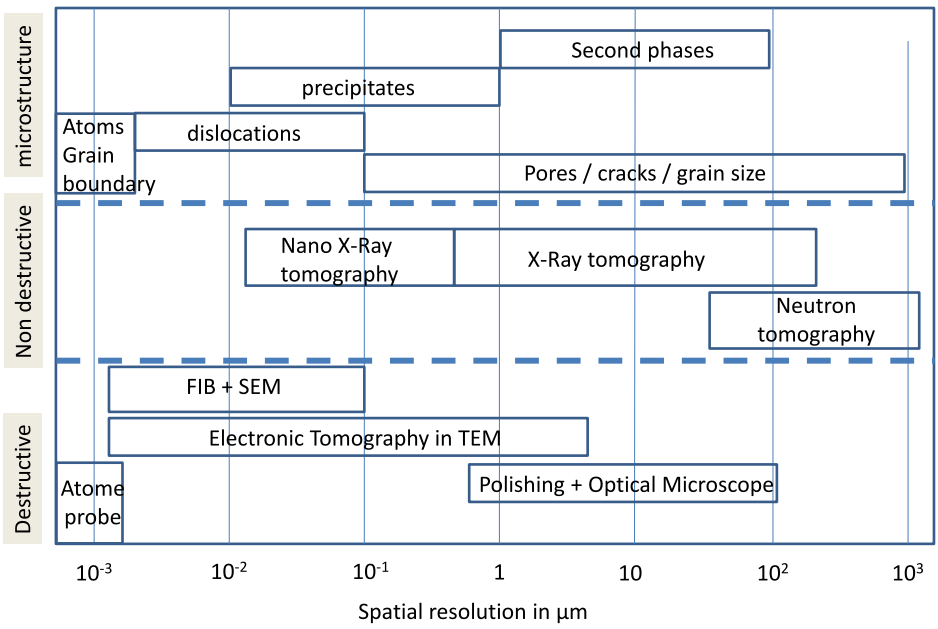

Fig. 1. Some 3D tools for 3D imaging in materials: non-destructive character and approximate spatial resolution.

scale of these microstructural features is shown in Fig. 1. In order to better understand the link between the microstructure and the properties of the materials it is necessary to obtain images of these features and to analyse them in a quantitative manner (number, size, volume fraction, connectivity, etc.). Thanks to microscopy it is possible to obtain 2D images of these features whatever their size: the optical microscope is used for features larger than 1 µm whereas the electronic microscopes (Scanning Electron Microscope, SEM or Transmission Electron Microscope, TEM) are used for smaller elements down to the nanometric scale. However, these techniques are destructive (the material need to be sectioned) and provide only 2D images on which some of the parameters cannot be determined: for example, the number of elements and their possible connectivity need 3D images. These limitations have led to the development of new tools to allow obtaining 3D images for a better representation of the microstructure. These tools can be classified according to the scales of observation and their ability to be non-destructive as shown in Fig. 1. These techniques are listed below; the reader is invited to read the special issue of Scripta Materialia [1] where these techniques are presented in details:

- The atom probe developed by [2] which allows investigating the spatial distribution of atoms in materials;
- The electron tomography [3], which allows imaging small precipitates;
- The Focus Ion Beam (FIB) used to make serial sections with a Scanning Electron Microscope (SEM) and explore a material in 3D with a high resolution [1];
- The mechanical polishing combined with optical microscopy or Electron Back Scattered Diffraction in an SEM which can reach a resolution of one micron [1,4];
- Neutron and X-ray tomography [1,4,5]. Nano X-ray tomography is a recent development.

Fig. 1 shows that X-ray tomography allows covering a wide range of microstructural feature observation with the additional advantage to be non-destructive.

2. X-ray tomography

2.1. Principle

Fig. 2a illustrates the principle of X-ray tomography: the specimen to be imaged is placed in the trajectory of an X-ray beam. Part of the X-rays is absorbed whereas the transmitted X-rays are converted into visible light using a scintillator. Thanks to a specific optics, a CCD or CMOS camera records this light which thus corresponds to a projection of the sample. The sample is then rotated over 180° or 360° and during this rotation, sufficient projections are recorded, normally several hundreds. This set of projections is usually named a scan; it is used to reconstruct a 3D image of the sample [6–8]. In the standard case where the sample is close to the camera, the contrast in the image is due mainly to the difference of the X-ray absorption coefficients between the various microstructural features present in the material. This absorption coefficient depends on the density of the material, the atomic number and the energy of the X-rays. In some cases, the absorption contrast is not sufficient: it is then possible to obtain phase contrast with a monochromatic beam by varying the distance

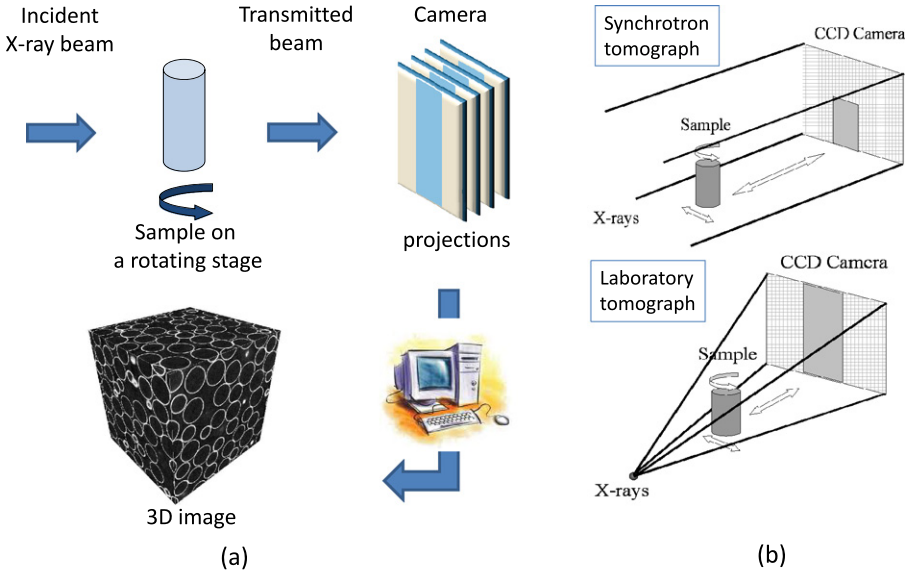

Fig. 2. (a) Principle of tomography; (b) Synchrotron and laboratory tomograph.

between the sample and the camera. The spatial resolution depends on the scintillator, on the optics used and on the pixel size of the camera. In order to obtain good quality 3D images it is necessary to fulfill several requirements:

- Transmission (ratio between the transmitted intensity and the initial intensity) must be large enough (above 20%). This transmission is mainly related to the energy of the X-rays, to the nature of the material and to the thickness of the sample;
- The number of projections should be high enough (theoretically equal to about 1.5 times the number of columns of the CCD camera but lower in practice);
- It is necessary to take images without the sample (flat field images) and images without the beam (dark field images) to make corrections of the projections.

There are two categories of tomographs (Fig. 2b): The laboratory tomographs where the X-ray beam is divergent and polychromatic, the spatial resolution varies from a few millimeters down to one micron (or less for new generation tomographs), and the typical acquisition time is approximately 15–30 minutes to obtain a 3D volume of $1024 \times 1024 \times 1024$ voxels. The synchrotron sources (ESRF, SOLEIL in France, SLS in Switzerland, Spring 8 in Japan, etc.) where the X-ray beam is parallel, polychromatic or monochromatic, the spatial resolution varies between 40 and 0.5 µm (around 50 nm in some cases) and the typical acquisition times is of the order of a few minutes (or even less than 1 s with fast cameras) to obtain a volume of $1024 \times 1024 \times 1024$ voxels.

2.2. X-ray tomography in materials science

X-ray tomography in material science is now becoming a conventional characterization technique which is confirmed by the number of articles published in international journals devoted to materials science (Scripta Materialia, Acta Materialia, Materials Science and Engineering A, etc.) with the keyword X-ray tomography: less than 10 before 2000 and about 80 in 2009. The main reason is that researchers often try to follow the microstructural evolution during heat treatment, mechanical testing (either at room or high temperature) and that relevant scales of the microstructure are of the order of microns which can be observed in any tomograph since 2000 [1]. There are several ways of doing tomography in materials science when the materials are subjected to heat treatment, mechanical testing at room or high temperature as shown in Fig. 3. In this figure, σ refers to mechanical testing and T to thermal treatment.

- *Post mortem tomography*: a scan is made at room temperature on a sample after heat treatment or mechanical testing. In order to study the influence of the thermal treatment or the mechanical test on the microstructure of the material, several samples must be used;
- *Ex situ tomography*: the procedure is the same as for post mortem tomography but the same sample is scanned. This requires sample cooling and reheating for thermal treatment and stress relaxation for mechanical testing, which may influence the mechanisms to be observed;

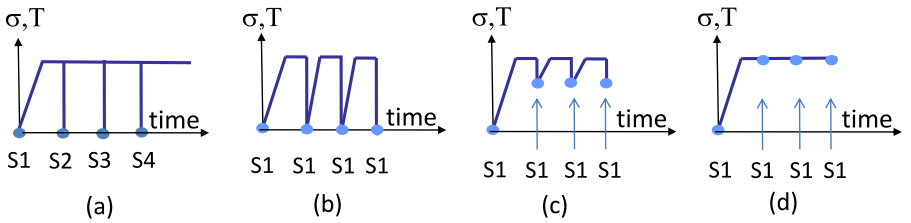

Fig. 3. (a) Post mortem; (b) Ex situ; (c) Interrupted in situ; (d) Continuous in situ.

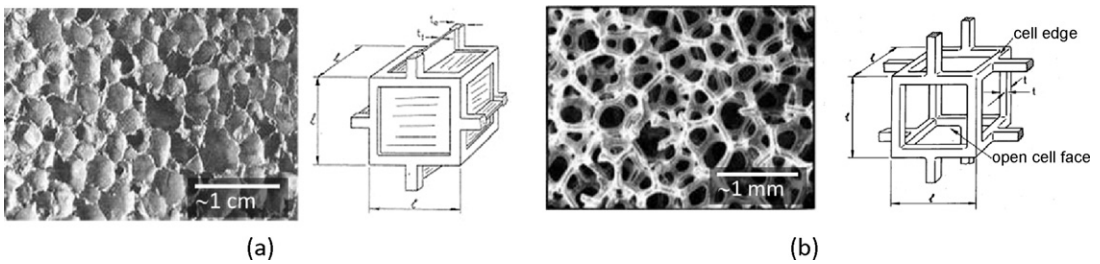

Fig. 4. (a) Closed-cell and its schematic representation; (b) Open cell foam and its schematic representation.

- *Interrupted in situ tomography*: the procedure is similar to ex situ tomography except that this technique requires specific testing devices (furnaces, compression–tension machine) mounted directly on the tomograph. The same sample is then scanned but mechanical tests need to be interrupted during the scan which again may affect the mechanisms;
- *Continuous in situ tomography*: in this procedure, the same sample is scanned without interrupting the mechanical test or the thermal treatment. This requires that the microstructure of the material does not change too much during the scan and therefore fast scans are often necessary.

3. Applications in materials science

We will present below two examples where the use of X-rays micro-tomography allows better understanding of physical mechanisms for a variety of materials in various loading conditions or thermal history. These examples are taken from research work of the authors and should not be considered as the only example of the use of micro-tomography in materials science. Readers may find other very interesting example in the following reviews [5,7,9,10].

3.1. 3D characterization of metal foams and modelling

3.1.1. Introduction

Metals foams are quite new materials even if some experiments to produce them were conducted in 1948 [11]. Academic studies rise up in 1995 because these materials combine a number of interesting physical properties and low density and thus may have great interest for weight reduction and also multi-functional applications [12,13]. The base metal use in these foams may be copper, steel, aluminium, magnesium or titanium but most studies were performed on aluminium metal foams for which a various processing routes exist. One can distinguish two subgroups: if the material is distributed in the faces and the struts of the cells, the foam is said to be *closed.* If it is in the struts only (so that the cells connect through open faces), the foam is said to be *open-celled*. Figs. 4a and 4b present images of such foams with their schematic representation introduced by Ashby et al. [14]. Intermediate configurations do exist (for example, cell faces are partly solid, or some faces are solid and others are open).

The main quantitative characteristic of a cellular material is its relative density $\rho = \rho^*/\rho_s$ where ρ^* is the density of the cellular material, and ρ_s the density of the constitutive material, i.e. the solid from which the cell walls and struts are made. What is important to notice is that physical properties are directly related to the relative density of the foams and of course the architecture of the foams. Concerning mechanical properties such as Young's modulus E^*, Ashby et al. [14] derived simple formulae using dimensional analysis.

$$\text{Open cell foam:} \quad E^* = BE_s\left(\rho^*/\rho_s\right)^2 \tag{1}$$

$$\text{Closed cell foam:} \quad E^* = CE_s\left(\phi\rho^*/\rho_s\right)^2 + DE_f(1-\phi)\left(\rho^*/\rho_s\right) \tag{2}$$

where B, C, D are constant and ϕ is the fraction of solids in the struts and E_s the Young's modulus of the struts and E_f the Young's modulus of the faces. Usually $E_s = E_f$ for most foams.

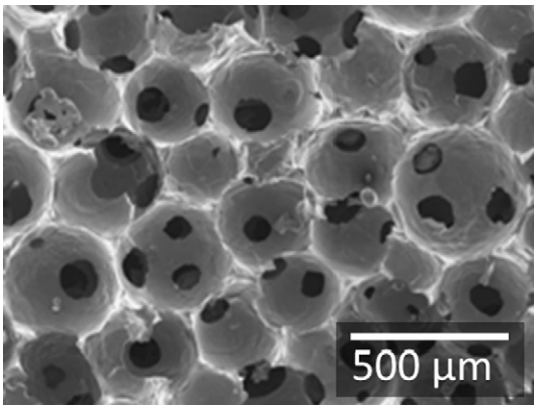

Fig. 5. SEM image of a replicated foam.

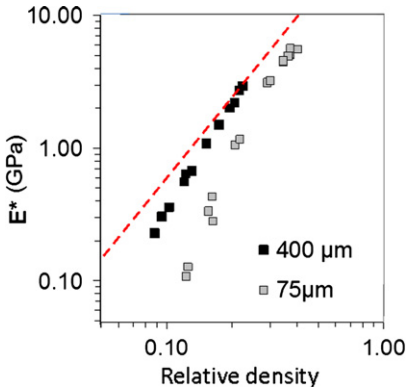

Fig. 6. Young's modulus versus relative density for two kind of replicated foams: dotted line represents Eq. (1).

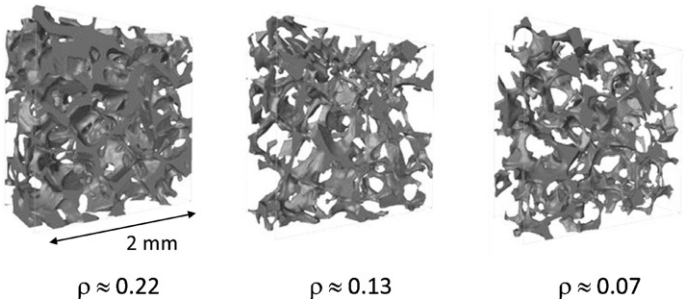

Fig. 7. 3D rendering of a 400 µm replicated foam for various relative densities.

3.1.2. Problematic

An old method to manufacture open cell foams has been improved at École polytechnique fédérale de Lausanne [15] and it relies mainly on several steps: compaction of salt particles (usually irregular) in order to obtain a preform, infiltration of the preform by pure aluminium or aluminium alloys under gas pressure, dissolution of the salt preform. Due to the compaction process the structure of the replicated metal foam is in between the open cell and the closed cell foam as shown in Fig. 5 and can be considered as partially closed cell. The relative density is changed as the compaction pressure is changed, thus it is possible to tailor the relative density of the foam. Furthermore when one look to the mechanical properties of these foam versus the relative density, it seems that the previous model does not describe well the foam behaviour whatever the size of the salt particles: either the exponent of the power is higher than expected (2.7 is found while the model predict 2), or a simple power law cannot retrieve experimental data as shown in Fig. 6 (where the dotted line represents a power law with exponent equal to 2, Eq. (1)). This remark is also true for other mechanical properties. The problematic is thus to understand this discrepancy with the usual model and if possible derive another model.

3.1.3. 3D characterization of the foam structure and modelling

We investigate the foam structure using the post mortem tomography. Various samples obtain for various compaction pressure (thus leading to various relative density) have been scanned at ESRF with spatial resolution adjusted to the size of the particles (2 µm for 75 µm particles and 10 µm for 400 µm particles). Fig. 7 presents 3D rendering of three foams with various relative densities and Fig. 8 a very simple schematic representation (struts are shown with constant thickness which is not the case). In order to characterize fully these foams one has to calculate the contact area A between cells, the number Z of contacts for each cells, usually called coordination number, the thickness of the struts and the length of the struts. Details to obtain these parameters have been given elsewhere [16].

These measurements allow to define an opening degree V of the foam by $V = ZA/\theta L^2$, where L is the strut length and a described the morphology of the cell which is not a cube but rather better represented by other polyhedral such as tetrakaidecahedron, rombohedral.

Fig. 9 presents V versus the relative density for the tow kind of foams. V is linear with density for 400 µm foams but presents a non-linear (or bilinear dependence) for the 75 µm foams: this has been attributed to rupture of salt particles during compaction to produce low density foams. If one comes back on Eq. (2), it is clear that since the faces present holes,

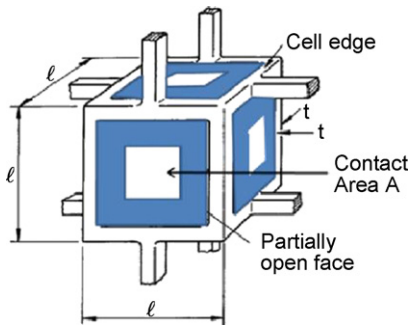

Fig. 8. Schematic representation of replicated foam.

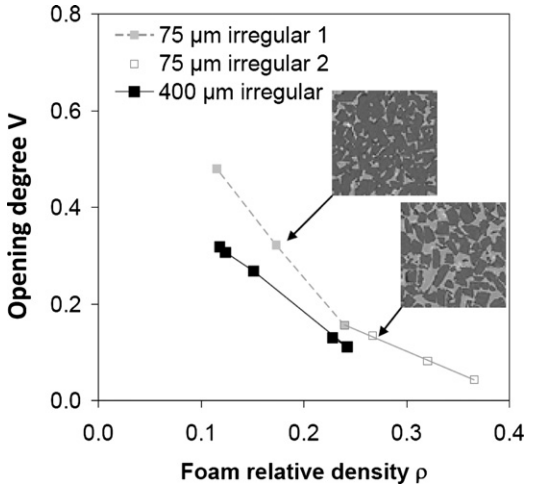

Fig. 9. Opening degree $V = ZA/\theta L^2$ as a function foam density for the two size foams.

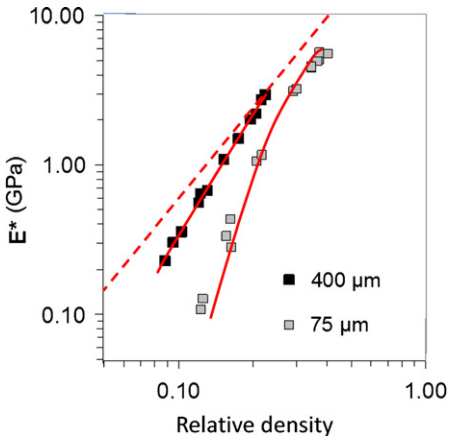

Fig. 10. Young's modulus versus relative density for two kind of replicated foams: dotted line represents Eq. (1) and the other two lines represent Eq. (3).

we cannot consider anymore that $E_s = E_f$. Micromechanics models allow predicting E_f as a function of V and E_s [17] and thus a corrected Young's modulus can be derived.

$$\text{Partially closed cell foam:} \quad E^* = CE_s\left(\phi\rho^*/\rho_s\right)^2 + D(1-\phi)\left(\rho^*/\rho_s\right)f(E_s, V) \tag{3}$$

Taking a very simple f function given by $f(E_s, V) = (E_s/(1-V))(1 - 1/(1 - V^{-0.5} + V^{-1}))$, and knowing the evolution of V with the relative density (Fig. 9) thanks to X-ray tomography and 3D image analysis, it is possible to better describe experimental data as shown in Fig. 10 and explain the discrepancies with the original Ahsby's model: for example, the fact that 75 µm foams do not have a power law dependency of the Young's modulus with density is related to rupture of particles during compaction process. This analysis is of course simplified since we consider that the struts present constant section, which we know that is not true and furthermore one more adjustable parameter θ is needed compare to Ashby's model. However this at least enables to catch a specific feature of replicated foams, namely their partially closed cell structure. It is possible to refine this analysis in order to catch all the features of the replicated foams and derive a model with a reduced number of adjustable parameters [18,19].

3.2. 3D solidification of aluminium alloys and modelling

3.2.1. Introduction

Melting and cooling down metals in order to produce casting parts is a very old technique in the human history since our ancestors were able to produce weapons [20]. The mass production of aluminium cast products starts more recently in 1886 with Hall–Héroult process of aluminium alloys leading to their application in aircraft industry and more recently

in train and automotive industry. However during the casting some defects (such as pores, cracks, intermetallics, etc.) may appear and lowered the mechanical properties of the alloys. The formation of defects in industrial metal casting processes due to various effects and one of them is the ability of the liquid to flow within the solid skeleton during the solidification of the materials [20,21]. For example, some aluminium alloys are known to be sensitive to hot tearing phenomenon (crack nucleation and propagation during solidification) and permeability, which characterized the liquid flow, is one of the parameters the influence this phenomenon [22–24]. The permeability K is derived from d'Arcy's Law assuming that solid velocity is and liquid body forces are negligible

$$V_l = (K/\mu_l)\nabla P_l \tag{4}$$

V_l is the liquid velocity, μ_l the liquid viscosity, ∇P_l the pressure gradient and K the permeability tensor. K is highly dependent on the solid fraction and it can be obtained experimentally though this is not easy for aluminium alloys [25]. Some analytical models exist to predict the influence of solid fraction and morphology of the solid on the permeability for isotropic materials. The most well-known relationship is the Carman–Kozeny equation [26] where

$$K = (1 - f_s)^3/\left(cS_v^2\tau^2\right) \tag{5}$$

where f_s is the solid fraction, c a constant, S_v the liquid–solid interface area over the volume and τ the tortuosity (average effective path of the liquid divided by the shortest path). Recently Nielsen et al. perform permeability measurements on Al–Cu alloys and found a very good correlation between experimental data and Carman–Kozeny data up to a fraction of solid of 0.85. Hot tearing phenomenon appears mainly at the end of solidification when the solid fraction is higher than 0.95 generally [24] and when one wants to model the nucleation of voids it is necessary to take into account the values of permeability at high solid fraction. The only way to do it is to use the Carman–Kozeny relationship and assume that it is still valid though there is no experimental data of permeability of aluminium alloys above a fraction of solid of 0.9.

3.2.2. Problematic

Recent 2D simulations [27] clearly show that in some cases the Carman–Kozeny model overestimates the permeability at high solid fraction. There is at the moment no experimental data to validate this discrepancy and when looking to Eqs. (4) and (5) it can be understood: at high solid fraction K is very low and is thus difficult to measure: at low pressure gradient the time to perform an experiment is too long and the solid structure may change during experiments. At high pressure gradient the time to perform an experiment is reduced, but this might induce solid network deformation and thus Eq. (4) is not valid anymore. In order to obtain permeability values at high solid fraction, we proposed to determine the 3D microstructure of the aluminium during solidification and to compute the permeability from these 3D data. This procedure has been validated on partially remelted Al–Cu alloys where experiments have been conducted [28]: the challenge is thus to obtain 3D data during solidification.

3.2.3. 3D characterization during solidification and modelling

It is not obvious to obtain full 3D characterization of aluminium alloys during solidification: indeed the materials changes during solidification and thus the time to acquire enough projections for 3D reconstruction may be too long. Thanks to development made at ESRF and specific furnaces that can be mounted on the tomography, it is possible to perform a complete scan in less than 30 s and thus if the solidification rate is slow it is possible to image the solidification in 3D continuously [29]. We performed the solidification of an Al–4%Cu at ESRF on ID19 beamline. The sample (1.5 mm in diameter) was held on a ceramic tube and a gas blower enables to heat the sample to liquid state and cooling down the sample at 3 °C/mn. The CCD FreLon Camera was set in high speed mode and a complete scan (acquisition of 400 radiographs) took approximately 20 s with an optic of 2.8 µm. 50 scans where recorded during solidification (from 660 °C down to 545 °C). Fig. 12 shows 2D section perpendicular to the axis of rotation of the sample during solidification from the liquid state. As an example Fig. 11 presents 2D slices during the solidification of an Al–4%Cu: at $T = 660$ °C the alloy is fully liquid, at $T + 645$ °C one can see the primary solid dendrites forming then growing as the temperature decreases and at 545 °C the material is fully solid.

Fig. 12 presents an extraction of the solid phase in 3D (the liquid has been made transparent) for various solid phase fraction. It is then possible from these 3D data to calculate S_v using marching cubes method [30], to compute the permeability as it is detailed in [28] and then to plot $K.S_v^2$ as a function of solid fraction. Fig. 13 presents the results of the simulation on the 3D data in the two main directions x and z (Kxx and Kzz) and the comparison with the conventional Carman–Kozeny law. It is also indicated the experimental data limit on the graph. Two interesting features can be drawn from these simulations:

- In the range of experimental data 3D simulation and Carman–Kozeny relationship present similar results thus validating the use of this analytical model in this range of solid fraction.
- Above a solid fraction of 0.85 there is a clear overestimation of the Carman–Kozeny relationship by a factor up to 10 at very high solid fraction.

This result on the overestimation of Carman–Kozeny law at high solid fraction is in accordance with 2D simulation [26]. This indicates that Carman–Kozeny assumption may not be valid at high solid fraction which is not surprising since this

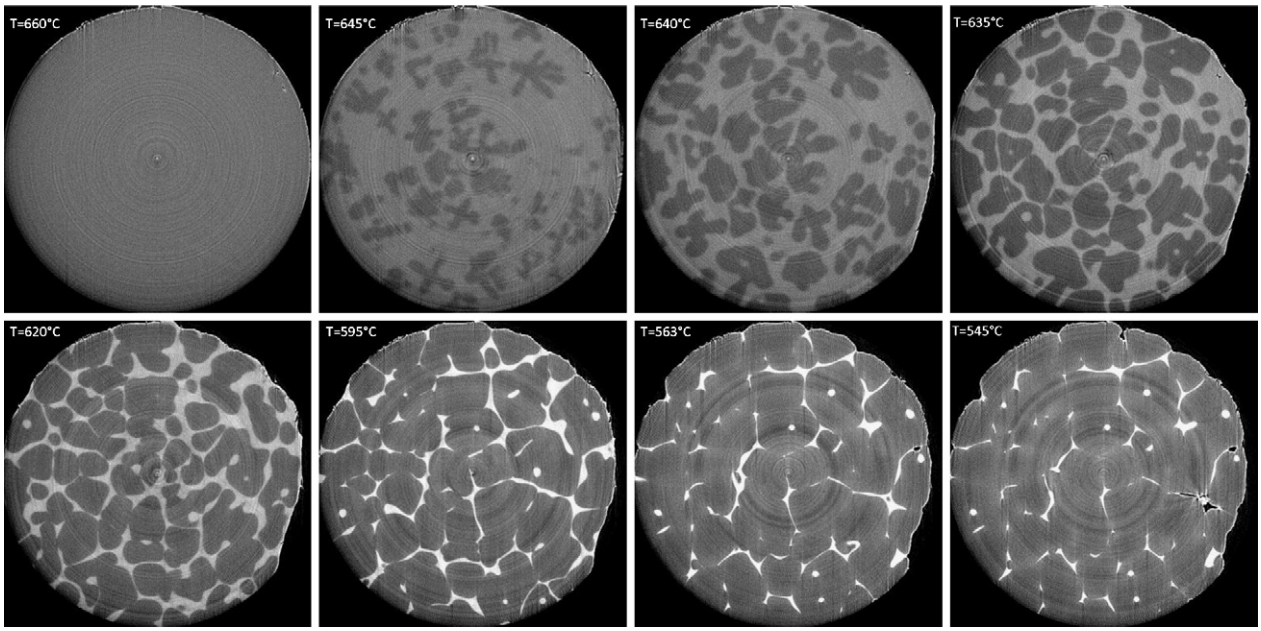

Fig. 11. 2D section of the solidification of an Al–4%Cu as a function of temperature: the diameter of the sample is 1.5 mm.

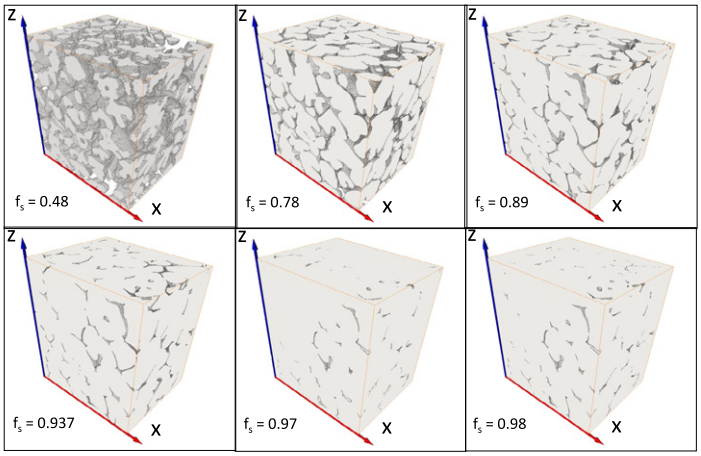

Fig. 12. 3D rendering of the solid phase as the solidification proceed (i.e. for various solid fraction): the height of the box is approximately 1.2 mm.

analytical model requires that there is no preferential path for the liquid flow through the solid which is hardly reasonable if one looks to the 3D structure of the material at high solid fraction (Fig. 12). Furthermore when looking carefully to liquid path, it seems that not all liquid fraction is available for the flow [31].

4. Conclusions

X-ray micro-tomography is a powerful tool to obtain 3D data with spatial resolution of the order of 1 µm. It is possible to perform scan on post mortem samples but also to perform in situ experiments while thermal treatment or mechanical treatment is applied to the material. 3D data obtained can be used to refine models or even to be input in 3D simulation. We presented two examples of the use of tomography in material science, which allowed to revisit classical issues with a new insight to test more refined models:

- For aluminium foams, 3D tomography data was used to better characterized the specific structure of replicated aluminium foams. This was used in order to refine Ashby's model which relate Young's modulus of the foam and relative density and to better describe experimental data;

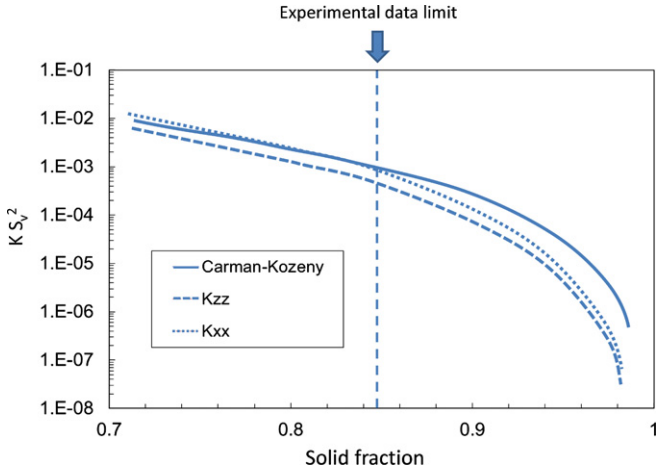

Fig. 13. Normalised permeability versus solid fraction: analytical model and 3D simulation from X-ray tomography data.

- For aluminium alloys, 3D in situ experiments were carried out to follow the solidification of Al–Cu alloys and compute the permeability as a function of solid fraction. It was shown that at high solid fraction, where experiments are difficult to realize, Carman–Kozeny law overestimates the permeability.

Acknowledgements

Authors would like to thank the team of ID19 at ESRF (Elodie Boller, Peter Cloetens, Wolfgang Ludwig) for X-ray tomography experiments. Grenoble INP is acknowledged for the grant that was given for a PhD to A. Marmottant in collaboration with EPFL (Andreas Mortensen). ANR is acknowledged for the support via a blank project TOMOSOLIDAL and the grant for N. Limodin.

References

[1] G. Spanos, Scripta Mater. 55 (1) (2006) 1–114.
[2] D. Blavette, B. Deconihout, A. Bostel, J.M. Sarrau, M. Bouet, A. Menand, Rev. Sci. Instrum. 64 (1993) 2911–2921.
[3] S. Benlekbir, T. Epicier, M. Bausach, M. Aouine, G. Berhault, Phil. Mag. Lett. 89 (2) (2009) 145–153.
[4] K. Thornton, H.F. Poulsen, Theme: three-dimensional materials science: an intersection of three-dimensional reconstructions and simulations, MRS Bull. 33 (6) (2008) 629.
[5] J. Baruchel, J.Y. Buffière, E. Maire, P. Merle, G. Peix, X-Ray Tomography in Material Science, Editions Hermes, 2000.
[6] P. Grangeat, La tomographie : fondements mathématiques, imagerie microscopique et imagerie industrielle, Traité IC2, série traitement du signal et de l'image, Editions Hermès, Lavoisier, 2002, 286 p.
[7] E. Maire, P. Merle, G. Peix, J. Baruchel, J.Y. Buffière, X-Ray Tomography in Material Science, Edition Hermes, 2000, 204 p.
[8] Di Michiel, L. Salvo, P. Cloetens, E. Maire, Techniques de l'ingénieur, IN20, 2004.
[9] F. Beckmann, R. Grupp, A. Haibel, M. Huppmann, M. Nöthe, A. Pyzalla, W. Reimers, A. Schreyer, R. Zettler, Adv. Eng. Mater. 9 (11) (2007) 939–950.
[10] L. Salvo, P. Cloetens, E. Maire, S. Zabler, J.J. Blandin, J.Y. Buffière, W. Ludwig, E. Boller, D. Bellet, C. Josserond, Nucl. Instrum. Methods Phys. Res. Sect. B: Beam Interact. Mater. Atoms 200 (2003) 273–279.
[11] B. Sosnick, United States Patent No. 2434775, 1948.
[12] L.-P. Lefebvre, J. Banhart, D.-C. Dunand, Adv. Eng. Mater. 10 (9) (2008) 775–787.
[13] M.F. Ashby, E.G. Evans, N.A. Fleck, L.J. Gibson, J.W. Hutchinson, H.N.G. Wadley, Metal Foams: A Design Guide, Butterworth Heinemann, 2000.
[14] L. Gibson, M.F.A. Ashby, Cellular Solids Structure and Properties, second ed., Cambridge University Press, Cambridge, UK, 1997.
[15] C. SanMarchi, A. Mortensen, Infiltration and the replication process for producing metal sponges, in: Handbook of Cellular Metals, Wiley-VCH Verlag, Weinheim, Germany, 2002, pp. 43–56 (Chapter 2.6).
[16] A. Marmottant, L. Salvo, C.L. Martin, A. Mortensen, J. Eur. Ceram. Soc. 28 (13) (2008) 2441–2449.
[17] S. Torquato, Random Heterogeneous Materials, Springer-Verlag, New York, 2002, 701 p.
[18] Y. Condé, Micro-, meso- and macrostructures in replicated microcellular aluminium, Ecole Polytechnique Fédérale de Lausanne, thesis no. 4308, 2009.
[19] Y. Condé, C. San Marchi, Andreas Mortensen, Acta Materialia, submitted for publication.
[20] M.C. Flemings, Solidification Processing, McGraw-Hill, New York, 1974, pp. 234–236.
[21] H.J. Thevik, A. Mo, T. Rusten, Metall. Mater. Trans. A 30B (1999) 135–142.
[22] M. Rappaz, J.-M. Drezet, M. Gremaud, Metall. Mater. Trans. A 30A (1999) 449–455.
[23] M. M'Hamdi, A. Mo, C.L. Martin, Metall. Mater. Trans. A 33A (2002) 2081–2093.
[24] J.A. Dantzig, M. Rappaz, Solidification: Methods, Microstructure and Modeling, EPFL Press, 2009, 620 p.
[25] Ø. Nielsen, L. Arnberg, A. Mo, H. Thevik, Metall. Mater. Trans. A 30A (1999) 2455–2462.
[26] P.C. Carman, Flow of Gases through Porous Media, Butterworth Scientific, London, 1956, pp. 11–13.
[27] S. Vernède, P. Jarry, M. Rappaz, Acta Mater. 54 (1) (2006) 4023–4034.
[28] D. Bernard, L. Salvo, Ø. Nielsen, P. Cloetens, Mater. Sci. Eng. A 392 (1–2) (2005) 112–121.
[29] O. Ludwig, M. DiMichiel, L. Salvo, M. Suéry, P. Falus, Metall. Mater. Trans. A 36 (2005) 1515.
[30] W.E. Lorensen, H.E. Cline, Comput. Graphics 21 (4) (1987).
[31] M. Suéry, J. Adrien, C. Landron, S. Terzi, E. Maire, L. Salvo, J.J. Blandin, Int. J. Mater. Res. 101 (2010) 1080–1088.